Yb^{2+}-doped $SrCl_2$: Electronic structure of impurity states and impurity-trapped excitons.

Goar Sánchez-Sanz,[1] Luis Seijo,[1,2] and Zoila Barandiarán[1,2]

[1]*Departamento de Química, C-XIV Universidad Autónoma de Madrid, 28049 Madrid, Spain*

[2]*Instituto Universitario de Ciencia de Materiales Nicolás Cabrera, Universidad Autónoma de Madrid, 28049 Madrid, Spain**

(Dated: July 12, 2010)

Abstract

First principles electronic structure calculations of the excited states of Yb^{2+}-doped $SrCl_2$ crystals up to 65000 cm^{-1} reveal the existence of unexpected excited states with double-well potential energy surfaces and dual electronic structure lying above and very close in energy to the $4f^{13}5d$ manifold, with which they interact strongly through spin-orbit coupling. The double-well energy curves result from avoided crossings between Yb-trapped exciton states (more stable at short Yb–Cl distances) and $4f^{13}6s$ impurity states (more stable at long Yb–Cl distances); the former are found to be pre-ionization states in which the impurity holds the excited electron in close lying empty interstitials located outside the $YbCl_8$ moiety. Spin-orbit coupling between the double-well states and lower lying $4f^{13}5d$ impurity states spreads the dual electronic structure character to lower energies and, hence, the instability of the divalent oxidation state is also spread. To some extent, the dual electronic structure (impurity-trapped exciton – impurity state) of some excited states expresses and gives support to hypotheses of interaction between Yb^{2+} and Yb^{3+} pairs proposed to understand the complex spectroscopy of the material and conciliates these hypotheses with interpretations in terms of the existence of only one type of Yb^{2+} defect. The results presented confirm the presence of impurity states of the $4f^{13}6s$ configuration among the $4f^{13}5d$ manifolds, as proposed in the literature, but their energies are very different from those assumed. The Yb-trapped excitons found in this chloride host can be seen as precursors of the luminescent Yb-trapped excitons characterized experimentally in the isomorphous SrF_2 crystals.

I. INTRODUCTION

The study of the energy levels of the $4f^{N-1}5d$ configuration of lanthanide containing materials has become a priority line of research due to their applications in solid state lighting,[1] lasers,[2] and other type of devices of technological significance. They are known to occur at much higher energies in the trivalent series (Ln^{3+}) than in the divalent series (Ln^{2+}) and this complementarity makes them even more attractive. As a result, the number of research reports showing increasingly sophisticated experimental studies, which reveal an underlying complex electronic structure and rich luminescent properties, is growing. Very often, as in the case of Yb^{2+}-doped $SrCl_2$ crystals, the spectroscopic properties of these materials were studied for the first time in the 1960s and 1970s,[3–5] with basic research points of view, to be almost completely ignored later on until the last few years, when they are being reinvestigated using advanced experimental techniques with the purpose of finding new and efficient materials for technological applications often related to energy handling and savings.[6] This renewed effort demands theoretical tools whose credit is comparable to the capabilities of nowadays experimental spectroscopy methods and whose ability to predict may help to guide and narrow the experimental search by building up new and more accurate models of their complex electronic structures. Consequently, we are conducting in our laboratory a number of *ab initio* quantum chemical studies of the electronic structure of the excited states of Ln^{3+} and Ln^{2+}-doped crystals to give unbiased non-empirical interpretations of the (expected and unexpected) electronic structures of the excited states of interest in basic and applied research.

This is particularly timely because theoretical interpretations within the framework of empirical crystal field theory (CFT) alone are very limited for several reasons. On the one hand, the $4f^{N-1}5d$ manifolds are usually very dense, very sensitive to chemical bonding, and only rarely is their vibrational structure unmasked for one or a few states, all of which makes the determination of crystal field parameters difficult, if not arbitrary, which often results in successive reassignments. On the other hand, the domain of CFT is basically confined to states of the $4f^N$ configuration and, with more difficulties, of the $4f^{N-1}5d$ configuration, so that spectral features associated with other electronic structures, which CFT can neither calculate nor predict, are either addressed resorting to related systems (typically, the free ions) or are catalogued as anomalous even when they are often found in the materials,

which indicates to what extent the theory has actually confined the way of thinking on their electronic structures. Yb^{2+}-doped $SrCl_2$ and SrF_2 crystals are good examples of all this, as explained next.

The absorption spectrum of $SrCl_2$:Yb^{2+} was measured by D. S. McClure and collaborators (Ref. 3) at very low temperature in the 1960s and interpreted in the framework of crystal field theory. This pioneering work was capable of detecting 12 peaks assigned to $4f^{14} \rightarrow 4f^{13}5d$ transitions. It pointed out an extensive configuration interaction between the $4f^{13}5d(e_g)$ and $4f^{13}5d(t_{2g})$ excited manifolds of Yb^{2+} in this cubic, fluorite-type crystal, induced by the comparable size of the spin-orbit coupling in the $4f^{13}$ shell and ligand field effects in the $5d$ shell. A study of photoluminescence spectra by the same group followed, which showed a highly complex luminescence behavior when the material was excited by near-ultraviolet radiation. This was not fully understood and raised the possibility of interaction between Yb^{2+} and Yb^{3+} centers.[4] The absorption spectrum was reinvestigated shortly after and a new, drastically different assignment was proposed by E. Loh (Ref. 5) on the basis of CFT, which assumed a much stronger crystal field splitting and the existence of three different types of Yb^{2+} sites and of Yb^{2+}–Yb^{3+} pairs. Much more recently, the absorption and emission spectra of Yb^{2+}-doped $SrCl_2$ were investigated again experimentally and with crystal field theory.[6] The absorption peaks observed in Ref. 3 were reassigned as a result of new CFT calculations which invoke the co-participation of the (low-lying) $4f^{13}6s$ configuration and rule out the existence of several Yb^{2+} centers suggested by Loh. The assignment of some peaks to the $4f^{13}6s$ configuration was done by inspection in Ref. 6, so that their energies match those of the $4f^{13}6s$ states in the Yb^{2+} free ion;[7] these peaks were left out of the crystal field fitting and of the calculation of the $4f^{14} \rightarrow 4f^{13}5d$ transitions, which reduced the root mean square deviations between experimental and CFT transition energies.[6] The study of the emission spectra at different temperatures deserved much attention in Ref. 6 and concluded that part of the emission bands detected in Ref. 4 do not belong to Yb^{2+}. Altogether, the detailed assignment and understanding of the absorption and emission spectra cannot be considered a solved and closed matter.

It is remarkable that the emission spectrum of Yb^{2+} changes drastically when the ion is doped in isomorphous SrF_2 instead.[8,9] In this case, it consists of two emission bands. One of them appears in the blue and is understood as the emission from the first $4f^{13}5d$ excited state; it roughly corresponds to the first absorption band of the material. The second

emission occurs in the red and was called "anomalous" when it was observed for the first time[8] because it is shifted by 2 eV from the first absorption band and is extremely wide; this emission is still called the anomalous emission of Yb^{2+} and similar signals have been detected in other hosts and are also produced by other divalent lanthanides, particularly by Eu^{2+}. They have been recently reviewed.[10] Other reasons why the red band was called and is still called anomalous are that it falls out of the framework and model that has been created for lanthanide ions in crystals using crystal field theory and because the electronic structure of such an excited state cannot be described nor predicted from it. Nevertheless, McClure and collaborators transcended the model and, from experiments alone, envisaged and described, with surprising precision, the characteristics of the electronic structure of the excited state responsible for the anomalous luminescence.[8] They called the excited state an "impurity-trapped exciton" since "it consists of a bound electron-hole pair with the hole localized on the impurity and the electron on nearby lattice sites"; furthermore, they predicted that the Yb–F bond length of such excited state should be close to that corresponding to the oxidized Yb^{3+} impurity.[8]

Taking all this into account, a number of questions arise such as: (i) whether impurity-trapped excitons exist also in the chloride and, if they do, how is their electronic structure and at what energies do they lie; (ii) whether the Yb^{2+} $4f^{13}6s$ states are in the $SrCl_2$ solid at similar energies above the ground state as in the free Yb^{2+} ion; (iii) how do impurity-trapped excitons and $4f^{13}6s$ states affect the expected location of the $4f^{13}5d$ configurations above the ground state; and (iv) what is their role in the interpretation of the spectroscopy of the $SrCl_2$:Yb^{2+} material. From the theoretical point of view, these questions can only be addressed if the theoretical model used is capable of generating both the expected and the anomalous electronic structures at once and from first principles alone. The objective of this paper is to to answer the first three questions formulated above and to start the analyses implied by the fourth by means of wave function based first-principles calculations on $(YbCl_8Sr_{12})^{18+}$ clusters embedded in $SrCl_2$. We present wave functions and energy curves of the excited states up to 65000 cm^{-1}. Their analyses indicate that impurity states of the $4f^{13}5d$ and $4f^{13}6s$ configurations coexist with unexpected impurity-trapped excitons and that they all interact strongly through spin-orbit, which spreads the characteristics of the unexpected electronic structures to energies involved in the experimental spectroscopy. The analyses show that the electronic structure of Yb^{2+}-doped $SrCl_2$ is far more complex than

expected from the available CFT empirical calculations to the point that only the lowest and the highest spin-orbit states found have a dominant single configurational character, whereas the rest exhibit mixed and dual electronic structures with extensive interactions and avoided crossings which result in fairly anharmonic and double-well potential energy surfaces. The main factors governing these complex interactions are extracted from the analyses presented in this paper and the main spectral features are addressed. The detailed absorption/emission spectroscopical analysis that emerges from the present calculations and its comparison with available experimental spectra are presented in a second paper.[11]

II. DETAILS OF THE CALCULATIONS

Since this paper is focused on describing in detail the wave functions and potential energy surfaces of the ground and excited states which are relevant for the spectroscopic properties of the Yb^{2+}-doped $SrCl_2$ material, we chose to use first-principles or *ab initio* quantum chemistry embedded cluster methods based on wave functions, because one of their strengths is their capability to calculate the potential energy surfaces of excited states of f-elements in solids, and another one is their ability to predict and model "unexpected" electronic structures (such as impurity-trapped excitons), if they exist in the material, in addition to "expected" electronic structures (such as states of $4f^N$, $4f^{N-1}5d$, or $4f^{N-1}6s$ configurations). Both capabilities are associated with the combination of molecular methods based on multireference wave functions[12–16] able to represent spin-orbit coupling and other relativistic effects,[17,18] with methods capable of representing quantum mechanical interactions between the cluster and the crystalline environment surrounding the point defect.[18,19] The methods have been described in their references and applications of them are readily found in the literature; therefore, we only give here the details necessary to reproduce the present calculations and to follow the text.

Yb^{2+} is supposed to substitute for Sr^{2+} ions in the cubic $SrCl_2$ crystal (ions and interstitial sites of the fluorite-like crystal, which are relevant for the discussions contained in this paper, are shown in Fig. 1). The defect is modelled by $(YbCl_8)^{6-}$ and $(YbCl_8Sr_{12})^{18+}$ cubic clusters subjected to the effects of the surrounding $SrCl_2$ crystal ions. Relativistic core *ab initio* model potentials (AIMP) have been used to represent the [Kr] core of Yb [20] and the [Ne] cores of Cl; [21] the corresponding Yb valence Gaussian basis set $(14s10p10d8f)$,[22] supplemented

with three g-type functions that give maximum radial overlap with the $4f$ atomic orbital, is contracted as $[6s5p6d4f1g]$; the Cl basis set used, $(7s7p1d)/[3s4p1d]$, includes one d-type polarization function[23] and one p-type diffuse function for anions;[24] the AIMPs and basis sets used for Sr are described in Sec. III A. The embedded cluster Hamiltonian includes the AIMP embedding potentials obtained in this work to represent the Sr^{2+} and Cl^{-} ions located at their cubic crystal structure sites (Group 225, $Fm\bar{3}m$, $a_0 = 6.9744$ Å[25]); the potentials were obtained by performing self-consistent embedded Sr^{2+} and Cl^{-} ions calculations at the Hartree-Fock level on the perfect host crystal as described in Ref. 18. All the ions located within a cube of length $4a_0$, centered at the impurity site, have been represented by AIMPs; point-charges have been used for the rest of ions located within a cube of length $7a_0$; fractional charges have been assigend to those located at the faces, edges, or corners of the outermost cube, following Evjen's method.[26]

Electron correlation and spin-orbit coupling have been combined following a two-step method.[27,28] In a first step, state-average complete active space self consistent field calculations (SA-CASSCF)[12] are performed using the spin-orbit free relativistic Wood-Boring AIMP Hamiltonian.[17] The active space used for the excited states results from distributing the 14 open-shell electrons in 13 active molecular orbitals with main character Yb $4f$, $5d$, and $6s$, which transform according to the a_{2u}, t_{1u}, t_{2u}, e_g, t_{2g}, and a_{1g} O_h point group irreducible representations. This space is the standard choice for a lanthanide[29] and generates about 10^5 configuration state functions in the D_{2h} point group in which the calculations were actually done. The molecular orbitals have been optimized in four separated SA-CASSCF calculations which minimize the average energy of: one $^3A_{1u}$, two $^3A_{2u}$, and three ^3E_u states; six $^3T_{1u}$ and five $^3T_{2u}$ states; and similarly for the spin singlets. These calculations are referred to as CASSCF($4f$,$5d$,$6s$) in the next Sections. For the ground state, the molecular orbitals were optimized in the single configuration $4f^{14}$–$^1A_{1g}$ closed shell. Alternatively, much simpler restricted active space SCF calculations (RASSCF) have been done in the ^3A_u D_{2h} symmetry block (which includes the $^3A_{1u}$, $^3A_{2u}$, and ^3E_u, O_h symmetry blocks) including one more a_{1g} active orbital and restricting the occupations so that 13 electrons are distributed in the a_{2u}, t_{1u}, t_{2u}, active orbitals, whereas only one electron can occupy the remaining e_g, t_{2g}, a_{1g}, and $a_{1g}{}'$ active orbitals; the state average of these RASSCF calculations was extended so as to include one more root of $^3A_{2u}$ symmetry. These RASSCF calculations have only been used to demonstrate the avoided crossings discussed in Sec. III A 3. Dynamic electron correlation

has been taken into account using the SA-CASSCF wave functions in subsequent multistate second-order perturbation theory calculations (MS-CASPT2),[13–16] where all 96 valence electrons were correlated; these calculations are referred to as MS-CASPT2(Cl64,Yb32). (It should be noted that the manifolds of excited states of f-elements are usually very dense and can lead to strong interactions and avoided crossings, as shown here. In cases similar to these, the MS-CASPT2 method has been shown to be a better alternative than the single-state (SS) CASPT2 method, because it allows for the mixing between SA-CASSCF wavefunctions at the second-order perturbation level through an effective Hamiltonian.[15,16,30]) A level shift of 0.1 au has been used in all intermediate SS-CASPT2 calculations to avoid the presence of intruder states.[31] The program MOLCAS has been used for these calculations.[32] In a second step, the full Wood-Boring AIMP Hamiltonian,[17] which includes the spin-orbit coupling operator (scaled by a factor of 0.9, as proposed in Ref. 33), has been used to perform double-group spin-orbit configuration-interaction (CI) calculations. The shifting operator included in this Hamiltonian, the so-called spin-free-state-shifting (sfss) operator,[27] transports the dynamic electron correlation effects retrieved at the spin-orbit free MS-CASPT2(Cl64,Yb32) level onto the smaller configurational space used in the spin-orbit CI calculations. This smaller space is formed by the $4f^{13}5d$ and $4f^{13}6s$ multireference plus all single excitations from the $4f$, $5d$, and $6s$ molecular orbitals to the virtual orbitals. Given that avoided crossings between states of the same symmetry were found to occur at different geometries in the MS-CASPT2 and in the smaller configurational space used in the spin-orbit CI calculations, the shifting parameters were carefully assigned by inspecting the electronic structure of the respective wave functions; in this way a correspondence between the states of the large and small spaces is established that obeys a criterium of maximum overlap rather than a criterium of energy order; the procedure followed has been described in detail elsewhere.[28] We refer to these calculations as sfss-SO-CI; they have been done using the EPCISO program.[34] All AIMP data (for embedding and/or for cores) and valence basis sets can be found in Ref. 35.

III. RESULTS AND DISCUSSION

As we will see, the complexity of the electronic structure of Yb^{2+}-doped $SrCl_2$ stems from two factors: On the one hand, the splittings due to ligand field effects on the $5d$ shell

and spin-orbit interactions within the $4f^{13}$ shell have similar magnitude, which results in extensive $4f^{13}5d(e_g) - 4f^{13}5d(t_{2g})$ configurational mixing, as expected.[3,6] On the other hand, the states of the the $4f^{13}6s$ configuration, which lie above the $4f^{13}5d(t_{2g})$ manifold and close in energy to it, exhibit unexpected double-well potential energy curves with dual electronic structure, which spin-orbit interaction spreads, affecting the wave functions and energy curves of lower lying electronic states. In order to unravel the final picture and identify the dominant factors, we analyze, in the next three subsections, the results of the methodological sequence: basic bonding interactions (Sec. III A), dynamic correlation (Sec. III B), and spin-orbit coupling (Sec. III C). In each case, the prominent methodological features and their physical meaning are highlighted, and their effects on the results are discussed. In all cases the effects of quantum mechanical embedding due to the $SrCl_2$ host and scalar relativistic effects are included in the calculations of wave functions and potential energy surfaces.

A. Basic bonding interactions: CASSCF calculations.

At the CASSCF level of methodology, only basic bonding interactions are modelled. On the one hand, the molecular orbitals of the $(YbCl_8Sr_{12})^{18+}$ cluster are expanded in terms of very flexible atomic basis sets, which allow for optimal mixings and deformations; on the other hand, the many-electron wave functions, are expanded in terms of a number of excited configurations involving the relevant open-shells of the material, which lie relatively close in energy and are allowed to interact in order to incorporate non-dynamic or static correlation between the valence open-shell electrons. At this stage, however, the energy of the excited states cannot be expected to be very precise since the dynamic correlation between the electrons is not well described. For this reason, the large energy difference between the $4f^{14}$ ground state and the excited states is not reproduced at this level of theory, as we will comment further in Sec. III B. Yet, the basic bonding and embedding interactions built in the CASSCF results usually give a very useful semiquantitative picture of the electronic structure. In the case of Yb^{2+}-doped $SrCl_2$, this picture is presented in Table I and in graphs (a) and (d) of Fig. 2.

The expected ligand field effects associated with bonding within the cubic $(YbCl_8Sr_{12})^{18+}$ cluster and interactions with the $SrCl_2$ embedding are clearly visible in Table I and Fig. 2 (a), where the lowest excited states can be grouped in two manifolds of nearly parallel energy

curves and main configurational character $4f^{13}5d(e_g)$ (ten levels) and $4f^{13}5d(t_{2g})$ (eighteen levels), in increasing energy order, whose bond lengths appear at shorter (3.041 Å) and longer (3.095 Å) values than the ground state bond length (3.076 Å), respectively, as it is usually found in f-element ions doped in crystals.[36,37] The peculiar shape of the energy curves of the states of the $4f^{13}6s$ configuration is also visible in Fig. 2 (a) and (d). They appear to have a long distance minimum at about 3.202 Å, a shoulder close to 2.9 Å, and significant configurational interaction with the highest members of the $4f^{13}5d(t_{2g})$ manifold at shorter distances deforming their potential energy surfaces. This interaction is particularly strong among 5^1T_{1u} and 6^1T_{1u} which also interact strongly at larger distance, so that two avoided crossings occur close to 2.84 and 3.07 Å that can be observed in detailed in graph (d) of Fig. 2, where only the ground state and all $^1T_{1u}$ excited states are plotted.

The shoulder was initially observed in the CASSCF curves of the highest states obtained using the smaller $(YbCl_8)^{6-}$ embedded cluster and the Yb$(14s10p10d8f3g)/[6s5p6d4f1g]$ and Cl$(7s7p1d)[3s4p1d]$ basis set described in Sec. II. Inspection of the wave functions at different Yb–Cl distances showed a significant change in electronic structure at either side of the shoulder, going from a localized $4f^{13}6s$ state at the longer Yb–Cl distances, to an impurity-trapped exciton analogous to that found in U^{4+}-doped Cs_2ZrCl_6 (Ref. 38) at the shorter distances. Given that the wave functions of impurity-trapped excitons have been shown to be somewhat delocalized,[38] we investigated the effects of enlarging the cluster and basis set sizes in two different ways in an attempt to reach a description of the two electronic structures (excitonic and local) reasonably close to convergence, as we comment below. It should be noted that the results presented in Table I and Fig. 2 correspond to the optimal choice of cluster and basis set investigated and therefore, can be considered reasonably close to convergence, as shown next.

1. Delocalization towards Sr next neighbours.

Following the experience gathered in the theoretical study of impurity-trapped excitons of U^{4+}-doped Cs_2ZrCl_6,[38] we enlarged the $(YbCl_8)^{6-}$ cluster so as to include the next 12 Sr^{2+} cations located at their $(\frac{1}{2},\frac{1}{2},0)$ next nearest neighbor sites in the $SrCl_2$ structure, in which Yb occupies the (0,0,0) site (see Fig. 1). Whereas all the occupied orbitals of the Sr^{2+} ions of the $(YbCl_8Sr_{12})^{18+}$ cluster were kept frozen and represented by the AIMP

embedding potential obtained for Sr^{2+} ions in the $SrCl_2$ crystal, the $4p$ occupied orbitals and empty $5s$ orbitals were used as valence basis set at these centers contracted as [ns1p]. The role of the $4p$ orbitals is to allow the molecular orbitals of the enlarged cluster to be orthogonal to the occupied and frozen Sr $4p$.[18] The role of the empty $5s$ orbitals is to enable delocalization of the cluster molecular orbitals towards the Sr sites if needed by the electronic structure. (These atomic orbitals were obtained performing one-electron calculations on the $5s$ – ^2S state of Sr^+ using the $11s$ primitive Gaussian basis functions of Sr from Ref. 21 plus an additional primitive with orbital exponent 0.01; the resulting $12s$ basis set was not contracted.)

The effects of splitting the Sr $5s$ atomic functions were investigated by allowing n to vary from 1 to 5; this leads to a series of [1s1p] to [5s1p] $(YbCl_8Sr_{12})^{18+}$ embedded cluster calculations. In all cases, the vertical transition energies to states representative of the $4f^{13}5d(e_g)$, $4f^{13}5d(t_{2g})$, and $4f^{13}6s$ manifolds were calculated at several Yb–Cl distances (shorter and longer than the distance at which the shoulder was observed); we show here only the short distance [R(Yb–Cl)=2.75 Å] results (see Table II and Fig. 3) because the effects were found to be negligible in the long distance calculations for all the transition energies mentioned. The effects of cluster and basis set extensions at 2.75 Å appear to be insignificant for all representative states other than the $2\ ^3A_{2u}$.

The above results show that delocalization is only useful for the $2\ ^3A_{2u}$ state when the Yb–Cl distance is shorter than that of the shoulder and that delocalization of its electronic structure results in stabilization of its relative energy.

2. Delocalization towards interstices.

The $YbCl_8$ moiety is surrounded by six empty interstices at ($\frac{1}{2}$,0,0), forming an octahedron around the Yb impurity in the fluorite-type $SrCl_2$ crystal (see Fig. 1). We have investigated the effects of locating basis functions at these empty sites in $(YbCl_8)^{6-}$ embedded cluster calculations. In particular, we have added n s-type primitive Gaussian functions which have been taken from the Sr($12s$) set referred above. We have used the last and most difuse Gaussian (n=1) of the Sr($12s$) set, the two last and most difuse Gaussians (n=2), and so on, to increase the flexibility of the cluster molecular orbitals and their ability to spread electronic density towards the interstices if required by the electronic structure. (The orbital

exponents of the Gaussians actually used are: 0.01, 0.02213, 0.05368, 0.31560, 0.70008). The calculations have been done on the same states at the same Yb–Cl distances as in Sec. III A 1. Again, we found that the basis set extensions were not needed at the long distance regime; therefore, we only show the short distance results in Table II and Fig. 3.

Delocalization towards the interstices appears to be demanded only by the electronic structure of the 2 $^3A_{2u}$ state at the short distance regime (last column in Table II and bullets in Fig. 3). This delocalization channel is found to be far more efficient in stabilizing the relative energy of the 2 $^3A_{2u}$ than delocalization towards Sr sites. The stabilization appears to be converged for n=4.

3. Charge leak across the $YbCl_8$ boundaries.

Finally, we combined the two previous extensions by calculating the transition energies on the enlarged cluster $(YbCl_8Sr_{12})^{18+}$ using the $[1s1p]$ and $[5s1p]$ bases at the Sr sites, and the $[4s]$ basis set at the interstices. The results corresponding to the short distance are presented in Table II and Fig. 3. Once more, the small effects on the transition energies to the states representative of the $4f^{13}5d(e_g)$ and $4f^{13}5d(t_{2g})$ manifolds, at short and long distances, and to the representative of the $4f^{13}6s$ configuration, at longer distance than the shoulder, revealed their localized nature. On the contrary, the results of the 2 $^3A_{2u}$ state at 2.75 Å show its delocalized nature. Interestingly, the stabilizations tabulated indicate again that the electronic structure of the 2 $^3A_{2u}$ prefers to spread its charge density across the faces of the Cl_8 cube towards the interstices, rather than across its edges towards the empty Sr orbitals. Furthermore, their convergence with basis set extensions suggests that, although part of the electronic density is spilled onto the surroundings of the $YbCl_6$ defect cluster, it is not detached from it. This is one of the reasons to identify this type of electronic structure with an impurity-trapped exciton.

Even though the preferred channel for delocalization is that connecting the Yb impurity with the interstices along (1,0,0) directions, we decided to keep the Sr channels [along (1,1,0) directions] opened with the minimal basis set $[1s1p]$ and all the calculations we present in this paper have been done in the $(YbCl_8Sr_{12})^{18+}$ embedded cluster using the Yb$(14s10p10d8f)/[6s5p6d4f1g]$, Cl$(7s7p1d)/[3s4p1d]$, Sr$(12s10p)/[1s1p]$, Interstice$[4s]$ basis, which amounts 320 basis functions. Finally, we checked the convergence of the combined

basis sets at the MS-CASPT2 level. The basis set effects are very similar to those we have just discussed at the CASSCF level; the values of the vertical transition to $2\ ^3A_{2u}$ at R(Yb–Cl)= 2.75 Å and their change are the following: Without basis set extensions: 59500 cm^{-1} (0); with Sr[1s1p] and Interstice[4s]: 50300 cm^{-1} (–9200); with Sr[5s1p] and Interstice[4s]: 49400 cm^{-1} (–10100).

In order to visualize the extent and topology of the charge spill, when it occurs, we have plotted the a_{1g} active molecular natural orbital of the $2\ ^3A_{2u}$ state in Fig. 4 at the two Yb–Cl distances indicated with vertical bars in the potential energy surface of plot (a). The 6s natural atomic orbital of the $4f^{13}6s$–^3F_u excited state of Yb^{2+} ion in the gas phase has also been plotted to set a reference [plot (b)]. We have chosen the diagonal plane of the Cl_8 cube so that the distribution of the natural orbital around two interstices (marked Int in the plots) and two Sr next neighbors, which are in plane, can be observed (see Fig. 1).

The delocalized/localized nature of the a_{1g} active molecular orbital can be deduced from Fig. 4 by comparing the plots (c) and (d), respectively, with the Yb–6s atomic orbital (b). The resemblance of the molecular and atomic orbitals at R(Yb–Cl)=3.18 Å is evident and this allows referring to this cluster orbital as the Yb–6s; conversely, it is so distorted at 2.75 Å that it cannot be associated with the Yb–6s orbital and we will refer to it as the a_{1g} active orbital of an Yb-trapped exciton, ${a_{1g}}^{YbTE}$, as we explain below. Its delocalization is quite evident and the charge leak across the $YbCl_8$ boundaries, preferentially across the faces, towards the interstices, is clear, which suggests that the charge delocalization occurs in such a way that proximity to the chlorines is avoided. As a matter of fact, the natural orbital shows a node at the cluster boundaries in the plane plotted. (It should be mentioned that the results shown here at 2.75 and 3.18 Å are representative of the abrupt change in electronic structure that occurs at other Yb–Cl distances at either side of the shoulder.)

This picture, together with the energy stabilization observed at short Yb–Cl distance, suggest the following evolution of interactions along the energy curve of $2\ ^3A_{1u}$: When the 4f electron is excited to the very diffuse Yb–6s orbital [Fig. 4, (b)] the interactions with the Cl_8 ligands cage and with the rest of the crystalline environment results in strong electron-electron repulsions which raise the energy of the $4f^{13}6s$ state relative to the free-ion energy and to other more localized excited states, as discussed in Ref. 39. This results in a very excited potential energy surface and long impurity–ligand bond length, as shown by the CASSCF results of Table I and Fig. 2. However, when the Yb–Cl distance decreases below a

critical distance of about 2.9 Å, electron-electron repulsion is abruptly reduced by the charge leaked from the Yb–6s to the ${a_{1g}}^{YbTE}$ orbital, where the excited electron, mainly localized on the ($\frac{1}{2}$,0,0) interstices, is still bound to the Yb $4f^{13}$ subshell (or, in other words, to the Yb $4f$ hole) in a preionization state. This sudden stabilization of the excited state energy below a critical distance is observed as a shoulder in the energy curve.

All together, the shoulder and the Yb-6s $\rightarrow$ ${a_{1g}}^{YbTE}$ redistribution of charge shown by the calculations indicate that an avoided crossing between two ${}^3A_{2u}$ electronic states with very different electronic structures occurs at a critical distance of 2.9 Å. [This avoided crossing has been calculated in detail with simpler restricted active space self-consistent field calculations, RASSCF, described in Section II, because calculating one additional state with one additional a_{1g} active orbital was extremely demanding. The result is shown in the inset of Fig. 2 (a) for the ${}^3A_{2u}$ symmetry. The same applies to all the states showing a shoulder]. One of the ${}^3A_{2u}$ states is the $4f^{13}6s$–${}^3A_{2u}$ state, which is more stable at R(Yb–Cl)>2.9 Å; the other one is the $4f^{13}{a_{1g}}^{YbTE\_}{}^3A_{2u}$ state, which is more stable at R(Yb–Cl)<2.9 Å; they only appear to interact at the avoided crossing critical distance. Furthermore, an analogous avoided crossing occurs at even shorter Yb–Cl distance between the $4f^{13}5d(t_{2g})$–${}^3A_{2u}$ and $4f^{13}{a_{1g}}^{YbTE\_}{}^3A_{2u}$ states which is accompanied, in this case, by Yb–$5d(t_{2g})$ $\rightarrow$ ${a_{1g}}^{YbTE}$ redistribution of charge.

The main reason to identify as "Yb-trapped excitons" the $4f^{13}{a_{1g}}^{YbTE\_}{}^{3,1}\Gamma$ (Γ=A_{2u}, T_{1u}, T_{2u}) electronic states which avoid crossing the $4f^{13}6s$ states, is that their electronic structure corresponds very closely to the type of excited state envisaged by McClure and Pédrini in Ref. 8, which the authors described as follows: "The excited state ... could be called an impurity-trapped exciton, since it consists of a bound electron-hole pair with the hole localized on the impurity and the electron on nearby lattice sites".

The results of the CASSCF calculations indicate that the flexibility of the basis sets used (even before the extensions discussed) allows one to detect interactions and avoided crossings between the local excited states of the $4f^{13}5d$ and $4f^{13}6s$ manifolds and impurity-trapped exciton states by the occurrence of shoulders in the energy curves of the former, accompanied by visible deformations of the active molecular orbitals at either side of the shoulder. This feature allows us to conclude with reasonable confidence that the only impurity trapped exciton states interacting with the local manifolds of Yb^{2+}-doped $SrCl_2$ correspond to the $4f^{13}{a_{1g}}^{YbTE}$ – ${}^{3,1}\Gamma$ manifold (Γ = A_{2u}, T_{1u}, T_{2u}).

As we discuss next, it is only when the correlation between interacting electrons is properly described that the excitonic electronic structure becomes stable and the $4f^{13}6s$ energy curves with shoulders become double-well potential energy surfaces.

B. Dynamic correlation: MS-CASPT2 calculations.

The correct description of the correlation in the movement of pairs of electrons occupying molecular orbitals of mainly Yb–$4f$ character is more demanding than that of $4f$–$5d$ and $4f$–$6s$ electron pairs because, given the different radial extent and angularity between the $4f$ and the $5d$ and $6s$ shells, the electron pairs are naturally further apart in the latter two cases. Consequently, the precision of the energy differences between the $SrCl_2$:Yb^{2+} $4f^{14}$ ground state and the states of the $4f^{13}5d$ and $4f^{13}6s$ manifolds, which are dominated by the excitation of an electron from the $4f$ to the $5d$ and $6s$ shells, respectively, depend strongly on a correct description of the differential dynamic correlation corrections, which stabilize the $4f^{14}$ ground state more strongly. This relative stabilization can be observed in the results of the MS-CASPT2 calculations of Table I and Fig. 2 (b) and (e), and it is responsible for widening the energy gap between the ground state and the remaining excited states from 2000 cm^{-1} (CASSCF result) to about 32000 cm^{-1} (MS-CASPT2 result). On the average, dynamic correlation increases the energy differences between the ground state and the states of the $4f^{13}5d(e_g)$, $4f^{13}5d(t_{2g})$, and $4f^{13}6s$ manifolds quite uniformly, by about 29600, 30000, and 31000 cm^{-1}, respectively (states 5^1T_{1u} and 6^1T_{1u} are excluded from these averages given their strong interaction observed at the CASSCF level, as discussed in Section III A).

For each individual state, dynamic correlation corrections usually increase with decreasing internuclear distances, which strengthens the bonds and makes equilibrium bond lengths noticeably shorter. This effect is observed here as follows: On the one hand, all the energy curves which show one minimum at the CASSCF level, shift their equilibrium distances to shorter values at the MS-CASPT2 level by an average of 0.12 to 0.14 Å, as shown in Table I for the ground state and the excited states of the $4f^{13}5d(e_g)$ and $4f^{13}5d(t_{2g})$ manifolds. On the other hand, the $4f^{13}6s$ energy curves, which show a shoulder at the CASSCF level, become double-well potential energy surfaces with the avoided crossing at 2.89 Å, as the short distance shoulder becomes a sharp maximum followed by a short distance minimum which is 3800–4800 cm^{-1} above the long distance minimum and around 2100 cm^{-1} lower

than the avoided crossing barrier. These energy curves show dual electronic structure, which changes from $4f^{13}6s$ to $4f^{13}{a_{1g}}^{YbTE}$ as the Yb–Cl distance becomes smaller than a critical distance where the avoided crossing takes place, as discussed above. The bond lengths, a_{1g} vibrational frequencies and energies of both electronic structures are given in Table I and Fig. 2 (b) and (e). Their interaction with states of the $4f^{13}5d(t_{2g})$ manifold of the same symmetry at distances longer and shorter than the critical one, respectively, can be observed in Fig. 2 (b) and is responsible for the large variation of the $\bar{\nu}_{a_{1g}}$ vibrational frequency values tabulated.

The energy differences between the spin singlet and triplet states tabulated in Table I for the two electronic structures indicate again that the excited electron is more delocalized in the $4f^{13}{a_{1g}}^{YbTE}$ impurity-trapped excitons than in the $4f^{13}6s$ states. In effect, they are much smaller for the excitonic states (where they are smaller that 250 cm^{-1}), suggesting that the interactions between the $4f^{13}$ and ${a_{1g}}^{YbTE}$ electronic densities are small and that they are far apart.

It is also very interesting to compare the R_e and $\bar{\nu}_{a_{1g}}$ values and the $T_e(T_{1u})$–$T_e(A_{2u})$ and $T_e(T_{2u})$–$T_e(A_{2u})$ energy differences for the spin triplet and spin singlet states of the $4f^{13}{a_{1g}}^{YbTE}$ impurity-trapped excitons in Table I with the following values that we obtained by equivalent MS-CASPT2 calculations on the trivalent ytterbium embedded cluster, $(YbCl_8)^{5-}$: R_e = 2.724, 2.726, 2.727 Å for $^2A_{2u}$, $^2T_{1u}$, and $^2T_{2u}$, respectively; $\bar{\nu}_{a_{1g}}$ = 260 cm^{-1} for the three states; and $T_e(^2T_{1u})$–$T_e(^2A_{2u})$=530 cm^{-1}, $T_e(^2T_{2u})$–$T_e(^2A_{2u})$=646 cm^{-1}. The similarities are very clear. In particular, the Yb–Cl bond lengths are very close, differing only by 0.06 Å. It is remarkable that this feature of impurity-trapped excitons showing impurity-ligand distances similar to those of the ionized impurity was also conjectured by McClure.[8]

Finally, before discussing the effects of spin-orbit coupling, we would like to remark that the equilibrium distances of all the states in the same manifold are very similar (Table I) because they all have approximately the same configurational character. Their sequence is as follows:

$$R_e\langle 4f^{13}a_{1g}^{YbTE}\rangle < R_e\langle 4f^{13}5d(e_g)\rangle < R_e\langle 4f^{14}\rangle < R_e\langle 4f^{13}5d(t_{2g})\rangle < R_e\langle 4f^{13}6s\rangle;$$

their values will help to visualize the configurational mixing induced by spin-orbit coupling, as we discuss next.

C. Spin-orbit coupling. Electronic structure of the excited states of Yb^{2+}-doped $SrCl_2$.

The results of the sfss-SO-CI calculations are presented in Table III and Fig. 2 (c) and (f). Comparison with those of the MS-CASPT2 calculations [Table I and Fig. 2 (b) and (e)] allow the determination of the effects of spin-orbit coupling on the electronic structure of the excited states. The dense spin-orbit energy curves are presented in more detail and separated according to their double group octahedral symmetry in Fig. 5 in order to show more clearly avoided crossings, anharmonicities, and double-well shapes.

The main effect of spin-orbit coupling is to induce a widespread and strong configurational mixing between the three manifolds of spin-orbit free states described above, so that only a few spin-orbit levels can be labeled with a dominant configurational character. This is due to two factors: On the one hand, spin-orbit coupling splits each manifold into two submanifolds due, basically, to the atomic splitting of the $4f^{13}$ subshell into $4f^{13}(J = 7/2)$ and $4f^{13}(J = 5/2)$ the splitting is of the order of 10000 cm^{-1} as can be deduced by comparing the energy curves of Fig. 2 with and without spin-orbit [graph (c) and (b), respectively]; analogous splittings were observed in Yb^{2+}-doped $CsCaBr_3$ where Yb^{2+} is in sixfold Br coordination.[40] On the other hand, the energy separation of the three spin-orbit free manifolds is much smaller than the spin-orbit splitting of their $4f^{13}$ subshell (in particular, ligand field splitting of the $5d$ shell and spin-orbit splitting of the $4f^{13}$ shell are found to be comparable, as expected[3]), therefore, their spin-orbit components overlap in energy and interact strongly through spin-orbit so that their different configurational character is lost in most cases.

In consequence, only two sets of states can be grouped and labeled by their main configurational character: the lowest $4f^{13}(7/2)5d(e_g)$ submanifold, whose energy curves are plotted in red in Fig. 2 (c), and the highest double-well submanifold $[4f^{13}(5/2)a_{1g}^{YbTE} - 4f^{13}(5/2)6s]$, whose energy curves are plotted in green in Fig. 2 (c). Within each of them, all states have very similar electronic structure and very similar bond length and a_{1g} vibrational frequency values which, in turn, are almost coincident with the respective values of their parent spin-orbit free states [cf. spin-orbit results in Table III and Fig. 2 (c) and (f), with MS-CASPT2 results in Table I and Fig. 2 (b) and (e)]. On the contrary, the interaction between states of the $4f^{13}(5/2)5d(e_g)$ and $4f^{13}(7/2)5d(t_{2g})$ submanifolds, on the one hand, and of the

$4f^{13}(5/2)5d(t_{2g})$ and the double-well $[4f^{13}(7/2)a_{1g}^{YbTE}$ – $4f^{13}(7/2)6s]$ submanifolds on the other, is so strong that nearly all states lose their former configurational character and show largely distorted potential energy surfaces, relative to their spin-orbit free parent states. A significant outcome of this is that the interaction between Yb-trapped exciton states and local impurity states is enhanced by spin-orbit coupling as it involves more excited states and occurs at lower energies as we show below.

In effect, the bond lengths of the states corresponding to the interacting $4f^{13}(5/2)5d(e_g)$ and $4f^{13}(7/2)5d(t_{2g})$ submanifolds, whose energy minima lie between 37000 and 45000 cm^{-1}, take intermediate values: $R_e[4f^{13}5d(e_g)] = 2.899$ Å$< R_e <R_e[4f^{13}5d(t_{2g})] = 2.967$ Å, their curvatures close to the minimum are notably variable, resulting in a wide range of values for their totally symmetric vibrational frequencies (Table III), and, in a few cases, show avoided crossings which lead to quite anharmonic potential energy surfaces, all of which can be appreciated in Fig. 5 between the auxiliary horizontal lines at 37000 and 46000 cm^{-1}. Interaction of the higher states in this group with the $4f^{13}(7/2)6s$ submanifold is also apparent at long distances; however, this interaction does not affect the characteristics of their equilibrium structures: neither the R_e and $\bar{\nu}_{a_{1g}}$ values nor their electronic structure.

The deformations of the potential energy surfaces resulting from the configurational mixing induced by spin-orbit coupling between the $4f^{13}(5/2)5d(t_{2g})$ and the double-well $[4f^{13}(7/2)a_{1g}^{YbTE}$ – $4f^{13}(7/2)6s]$ states are more profound and are best described by the potential energy curves themselves, whose energy minima lie between 47000 and 54000 cm^{-1}, and are grouped by symmetries in Fig. 5 where they are delimited by the auxiliary lines at 46000 and 58000 cm^{-1}. The avoided crossings are very common and, often, multiple, because the double-well structure of the $[4f^{13}(7/2)a_{1g}^{YbTE}$ – $4f^{13}(7/2)6s]$ states provokes strong interactions at both short and long distances with states of the $4f^{13}(5/2)5d(t_{2g})$ submanifold and with the higher states of the $4f^{13}(7/2)5d(t_{2g})$ submanifold [this is best appreciated when graphs (b) and (c) of Fig. 2 are compared]. We have plotted states $6A_{1u}$ and $5A_{2u}$ using dashed lines in Fig. 5 in the less dense A_{1u} and A_{2u} symmetry graphs to stress the avoided crossings, but they are also quite evident and abundant in the remaining E_u, T_{1u}, and T_{2u} blocks as well. As a consequence, the lowest energy minima collected in Table III are often followed, at shorter Yb–Cl distances, by (smaller/larger) energy barriers leading to a variety of shapes: a second, short distance minimum, or one or several shoulders. Consequently, the meaning of the parameters extracted from regressions of the energy *vs*. Yb–Cl

distance numerical values closest to the lower minima, for each state, presented in Table III, has to be put in perspective, taking into account the shape of the whole numerical energy curve shown in the figures presented in this paper. The analysis of the wave functions presented in Table III indicate the electronic structure of each state at and close to the Yb–Cl distance used to calculate it, however it should be taken into account that the electronic structure closely follows the abrupt changes observed in the potential energy surfaces. In order to illustrate this we have tabulated the wave function analyses of $5A_{1u}$, $6A_{1u}$, and $7A_{1u}$ at different Yb–Cl distances in Table IV. These states are also good examples of the spin-orbit induced interaction between Yb-trapped exciton states and local impurity states lying at lower energies, mentioned above, so widespread in this portion of the spectrum. Given that the impurity-trapped exciton states can be considered preionization states due to their shown relatively delocalized electronic structure, their significant contribution to a number of excited states of Yb^{2+}-doped $SrCl_2$ indicates that the divalent oxidation state is somewhat unstable at energies higher than about 50000 cm^{-1}. Furthermore, the spin-orbit enhanced mixing between Yb-trapped exciton states and Yb^{2+} local states gives shape to the hypotheses of some sort of interaction between Yb^{2+} and Yb^{3+} centers proposed to explain the complex spectroscopy of $SrCl_2$:Yb^{2+} (Refs. 4, 5) at the same time that it is compatible with the conclusion that the absorption spectrum is entirely due to Yb^{2+} (Ref. 6).

IV. CONCLUSIONS

We have calculated and analyzed the spin-orbit, correlated wave functions and potential energy surfaces of excited states of Yb^{2+}-doped $SrCl_2$ crystals up to 65000 cm^{-1} above the ground state using first-principles embedded cluster methods based on wave functions. Their electronic structures appear to be more complex than initially expected so that only the lowest and highest spin-orbit states have a dominant configurational character, whereas the rest exhibit fairly anharmonic and double-well potential energy surfaces with mixed and dual electronic structure, respectively, due to extensive avoided crossings and interactions. The main factors governing these complex structures are the following: (1) The splittings due to ligand field effects on the $5d$ shell and spin-orbit coupling within the $4f^{13}$ shell have similar magnitude, which results in extensive $4f^{13}5d(e_g)$ – $4f^{13}5d(t_{2g})$ configurational mixing when spin-orbit coupling is introduced in the calculations, as expected on the basis of previous

work.[3,6] (2) The calculations without spin-orbit reveal the existence of excited states with unanticipated double-well potential energy curves and dual electronic structure lying above and very close in energy to the $4f^{13}5d(t_{2g})$ manifold, which result from avoided crossings at a critical Yb–Cl distance of 2.89 Å between $4f^{13}a_{1g}$ Yb-trapped exciton states (more stable at short Yb–Cl distances) and $4f^{13}6s$ states (more stable at long Yb–Cl distances); their excited electron appears to be significantly localized outsite the $YbCl_8$ volume, on the six next nearest empty interstitial sites of the fluorite-type structure, or within the $YbCl_8$ moiety, respectively; and their bond lengths appear to be very close to those of the Yb^{3+}-doped $SrCl_2$ ground configuration or the longest of all excited states of the Yb^{2+}-doped crystal, respectively. (3) Spin-orbit spreads the interaction between Yb-trapped excitons and local impurity states to lower energy regions by inducing the coupling between the double-well states with lower lying members of the $4f^{13}5d(t_{2g})^1$ and $4f^{13}5d(e_g)^1$ manifolds; in consequence, a number of spin-orbit excited states also show anharmonic and double-well energy curves.

The Yb-trapped excitons found in this work are preionization states (the electron is found to be still bound to the impurity) and reveal that the divalent oxidation state is unstable, to some extent, above 50000 cm^{-1} and at Yb–Cl distances smaller than a critical value of 2.89 Å. Their electronic structure is fairly different from the impurity-trapped excitons found in U^{4+}-doped Cs_2GeF_6 crystals.[38] Whereas the latter can be described as very diffuse $5f^17s^1$ states, the former are very different from the $4f^{13}6s^1$ states; rather, they appear to be new excited states which suggest, more closely, the idea of a conduction band electron trapped by the oxidized impurity, which, in addition, interact with $4f^{13}6s^1$ and other lower impurity states, avoiding crossings.

The double-well and dual electronic structure (Yb-trapped exciton – impurity state) characteristics of many excited states can be viewed as an expression of the hypotheses of interaction between Yb^{2+} and Yb^{3+} centers proposed to understand the complex spectroscopy of this material in previous works.[4,5]

Acknowledgments

This research was supported in part by the Ministerio de Ciencia e Innovación, Spain, under contract MAT2008-05379. G.S-S. acknowledges an FPI fellowship from Ministerio de

Ciencia e Innovación, Spain.

---

* Corresponding author; Electronic address: zoila.barandiaran@uam.es

[1] J. Y. Tsao, IEEE Circuits & Devices **20**, 28 (2004).

[2] S. Kück, Appl. Phys. B **72**, 515 (2001).

[3] T. S. Piper, J. P. Brown, and D. S. McClure, J. Chem. Phys. **46**, 1353 (1967).

[4] H. Witzke, D. S. McClure, and B. Mitchell, in *Luminescence of Crystals, Molecules, and Solutions*, edited by F. E. Williams (Plenum, New York, 1973), p. 598.

[5] E. Loh, Phys. Rev. B **7**, 1846 (1973).

[6] Z. Pan, C. Duan, and P. A. Tanner, Phys. Rev. B **77**, 085114 (2008).

[7] B. W. Bryant, J. Opt. Soc. Amer. **55**, 771 (1965).

[8] D. S. McClure and C. Pédrini, Phys. Rev. B **32**, 8465 (1985).

[9] B. Moine, C. Pédrini, D. S. McClure and H. Bill, J. Lumin. **40&41**, 299 (1988).

[10] P. Dorenbos, J. Andriessen, and C. W. E. van Eijk, J. Solid State Chem. **171**, 133 (2003).

[11] G. Sánchez-Sanz, L. Seijo, and Z. Barandiarán, in preparation.

[12] B. O. Roos, P. R. Taylor, and P. E. M. Siegbahn, Chem. Phys. **48**, 157 (1980); P. E. M. Siegbahn, A. Heiberg, J. Almlöf, and B. O. Roos, J. Chem. Phys. **74**, 2384 (1981); P. Siegbahn, A. Heiberg, B. Roos, and B. Levy, Phys. Scr. **21**, 323 (1980).

[13] K. Andersson, P.-Å. Malmqvist, B. O. Roos, A. J. Sadlej, and K. Wolinski, J. Phys. Chem. **94**, 5483 (1990).

[14] K. Andersson, P.-Å. Malmqvist and B. O. Roos, J. Chem. Phys. **96**, 1218 (1992).

[15] A. Zaitsevskii and J. P. Malrieu, Chem. Phys. Lett. **233**, 597 (1995).

[16] J. Finley, P.-Å. Malmqvist, B. O. Roos and L. Serrano-Andrés, Chem. Phys. Lett. **288**, 299 (1998).

[17] L. Seijo, J. Chem. Phys. **102**, 8078 (1995).

[18] L. Seijo and Z. Barandiarán, in *Computational Chemistry: Reviews of Current Trends*, edited by J. Leszczyński (World Scientific, Singapore, 1999), vol. 4, p. 55.

[19] Z. Barandiarán and L. Seijo, J. Chem. Phys. **89**, 5739 (1988).

[20] L. Seijo, Z. Barandiarán, and B. Ordejón, Mol. Phys. **101**, 73 (2003).

[21] Z. Barandiarán and L. Seijo, Can. J. Chem. **70**, 409 (1992).

[22] L. Seijo, Z. Barandiarán, and E. Harguindey, J. Chem. Phys. **114**, 118 (2001).

[23] J. Andzelm, M. Klobukowski, E. Radzio-Andzelm, Y. Sakai, and H. Tatewaki, *Gaussian Basis Sets for Molecular Calculations*, edited by S. Huzinaga, (Elsevier, Amsterdam, 1984).

[24] T. H. Dunning and P. J. Hay, in *Modern Theoretical Chemistry*, edited by H. F. Schaefer III (Plenum, New York, 1977).

[25] R. W. G. Wyckoff, *Crystal Structures*, vol. 1, 2nd. edn. (Interscience Publishers, 1982).

[26] H. M. Evjen, Phys. Rev. **39**, 675 (1932).

[27] R. Llusar, M. Casarrubios, Z. Barandiarán, and L. Seijo, J. Chem. Phys. **105**, 5321 (1996).

[28] G. Sánchez-Sanz, Z. Barandiarán, and L. Seijo, submitted.

[29] L. Seijo and Z. Barandiarán, J. Chem. Phys. **118**, 5335 (2003).

[30] J.-P. Malrieu, J.-L. Heullly, and A. Zaitzevskii, Theor. Chim. Acta **90**, 167 (1995).

[31] B. O. Roos and K. Andersson, Chem. Phys. Lett. **245**, 215 (1995).

[32] G. Karlström, R. Lindh, P. A. Malmqvist, B. O. Roos, U. Ryde, V. Veryazov, P. O. Widmark, M. Cossi, B. Schimmelpfennig, P. Neogrady, and L. Seijo, Comput. Mater. Sci. **28**, 22 (2003).

[33] Z. Barandiarán and L. Seijo, J. Chem. Phys. **118**, 7439 (2003).

[34] V. Vallet, L. Maron, C. Teichteil, and J.-P. Flament , J. Chem. Phys. **113**, 1391 (2000).

[35] Detailed core and embedding AIMP data libraries in electronic format are available from the authors upon request or directly at the address http://www.uam.es/quimica/aimp/Data/-AIMPLibs.html. See also Ref. 32.

[36] Z. Barandiarán and L. Seijo, J. Chem. Phys. **119**, 3785 (2003).

[37] Z. Barandiarán, N. M. Edelstein, B. Ordejón, F. Ruipérez, and L. Seijo, J. Solid State Chem. **178**, 464 (2005).

[38] B. Ordejón, L. Seijo, and Z. Barandiarán, J. Chem. Phys. **126**, 194712 (2007).

[39] G. Sánchez-Sanz, L. Seijo, and Z. Barandiarán, Spec. Letters, in press.

[40] G. Sánchez-Sanz, L. Seijo, and Z. Barandiarán, J. Phys. Chem. A **113**, 12591 (2009).

TABLE I: Spectroscopic constants of the ground and excited states of the $(YbCl_8Sr_{12})^{18+}$ cluster embedded in $SrCl_2$. Spin-free Hamiltonian calculations. Yb–Cl bond distances, R_e, in Å; totally symmetric vibrational frequencies, $\bar{\nu}_{a_{1g}}$, in cm^{-1}; and adiabatic energy differences, T_e, relative to the $4f^{14}$–1^1A_{1g} ground state, in cm^{-1}. Manifold averages and mean square deviations of the individual values with respect to the averages are labeled as $\langle 4f^{13}5d(e_g)\rangle$, $\langle 4f^{13}5d(t_{2g})\rangle$, and $\langle 4f^{13}6s\rangle$.

	CASSCF($4f$,$5d$,$6s$) [1,2]			MS-CASPT2(Cl64,Yb32)		
state	R_e	$\bar{\nu}_{a_{1g}}$	T_e	R_e	$\bar{\nu}_{a_{1g}}$	T_e [3]
$1\ ^1A_{1g}$	3.076	174	0	2.954	184	0
$\langle 4f^{13}5d(e_g)\rangle$	3.041±0.003	177±1		2.899±0.004	203±5	
$1\ ^3T_{1u}$	3.045	176	1987	2.904	198	32287
$1\ ^3T_{2u}$	3.040	177	5109	2.899	205	34803
$2\ ^3T_{1u}$	3.042	177	6263	2.901	202	35592
$1\ ^1T_{2u}$	3.039	178	6299	2.899	205	35760
$1\ ^3E_u$	3.041	177	6168	2.903	196	36837
$1\ ^1E_u$	3.039	177	6940	2.900	200	37026
$1\ ^1T_{1u}$	3.044	176	7930	2.897	197	37252
$2\ ^3T_{2u}$	3.038	178	8830	2.896	210	37459
$2\ ^1T_{1u}$	3.043	177	8402	2.892	208	38213
$2\ ^1T_{2u}$	3.036	178	9440	2.896	209	38296
$\langle 4f^{13}5d(t_{2g})\rangle$	3.095±0.002	173±2		2.967±0.001	182±2	
$3\ ^3T_{1u}$	3.092	175	10444	2.967	183	41333
$4\ ^3T_{1u}$	3.092	175	14184	2.967	182	44285
$2\ ^3E_u$	3.094	174	13781	2.967	182	44781
$3\ ^3T_{2u}$	3.094	174	13989	2.968	182	44993
$2\ ^1E_u$	3.096	174	14701	2.968	182	45189
$3\ ^1T_{2u}$	3.096	174	15084	2.968	182	45499
$1\ ^3A_{2u}$	3.096	173	16193	2.967	182	45859
$3\ ^1T_{1u}$	3.092	175	16547	2.965	182	46257
$4\ ^3T_{2u}$	3.095	174	17111	2.968	182	46987
$3\ ^1E_u$	3.094	174	17636	2.965	182	47353
$5\ ^3T_{1u}$	3.094	174	18454	2.966	182	47585
$3\ ^3E_u$	3.093	174	17563	2.967	181	47746

4 $^1T_{1u}$	3.095	173	18710	2.964	181	47786
1 $^1A_{1u}$	3.096	173	18675	2.968	183	47978
1 $^3A_{1u}$	3.096	173	18693	2.966	184	48360
5 $^1T_{1u}$	3.202 [2]	180 [2]	21980	2.965	182	48566
1 $^1A_{2u}$	3.099	169	19437	2.969	174	48981
4 $^1T_{2u}$	3.097	171	19279	2.968	179	49005

States with double-well potential energy surfaces

				Long distance minimum		
$\langle 4f^{13}6s\rangle$ [1]	3.202±0.006	181±12		3.076±0.003	182±8	
2 $^3A_{2u}$	3.207	170	21380	3.077	176	52765
6 $^3T_{1u}$	3.206	176	21032	3.079	176	52772
5 $^3T_{2u}$	3.207	170	21270	3.078	176	52838
2 $^1A_{2u}$	3.194	195	22444	3.070	196	53548 (783)
6 $^1T_{1u}$	3.096 [2]	251 [2]	24719	3.076	184	53702 (930)
5 $^1T_{2u}$	3.197	193	22275	3.077	183	53869 (1031)

	Short distance minimum		
$\langle 4f^{13}a_{1g}{}^{YbTE}\rangle$	2.789±0.003	285±25	
2 $^3A_{2u}$	2.784	236	57267
6 $^3T_{1u}$	2.790	241	57585
5 $^3T_{2u}$	2.791	238	57690
2 $^1A_{2u}$	2.791	296	57309 (42)
6 $^1T_{1u}$	2.789	258	57833 (248)
5 $^1T_{2u}$	2.789	278	57913 (223)

[1] At the CASSCF level, the states of the $4f^{13}6s$ manifold have a shoulder at about 2.9 Å and a minimum at the tabulated R_e values. At the MS-CASPT2 level, they show two energy minima whose data are tabulated.

[2] An avoided crossing occurs between 5^1T_{1u} and 6^1T_{1u} at the CASSCF($4f$,$5d$,$6s$) level; their R_e and $\bar{\nu}_{a_{1g}}$ values are not used to compute the manifold averages. See text for details.

[3] Adiabatic energy differences between spin singlet and spin triplet states are given in parentheses.

TABLE II: Effects of extensions to the Yb($14s10p10d8f3g$)/[$6s5p6d4f1g$], Cl($7s7p1d$)/[$3s4p1d$] basis set on the transition energy to representative electronic states of the $4f^{13}5d(e_g)$, $4f^{13}5d(t_{2g})$, and $4f^{13}6s$ manifolds computed at R(Yb–Cl)=2.75 Å. All numbers in cm^{-1}.

		vertical absorption from $4f^{14}$ – $^1A_{1g}$					
Cluster	basis extension	$4f^{13}5d(e_g)$	$4f^{13}5d(t_{2g})$				$4f^{13}6s$
		$1\ ^3E_u$	$2\ ^3E_u$	$1\ ^3A_{2u}$	$3\ ^3E_u$	$1\ ^3A_{1u}$	$2\ ^3A_{2u}$
$(YbCl_8)^{6-}$	None	2635	16319	18689	19838	21092	30305
$(YbCl_8Sr_{12})^{18+}$	at ($\frac{1}{2}$,$\frac{1}{2}$,0) Sr sites						
	[$1s1p$]	2617	16061	18390	19519	20752	28603
	[$2s1p$]	2480	16113	18449	19579	20817	28045
	[$3s1p$]	2353	16202	18547	19678	20923	27750
	[$4s1p$]	2222	16230	18576	19705	20952	27191
	[$5s1p$]	2232	16230	18576	19705	20953	27227
$(YbCl_8)^{6-}$	at ($\frac{1}{2}$,0,0) Interstices						
	$1s$	2624	16321	18691	19840	21094	29804
	$2s$	2578	16327	18698	19846	21101	28377
	$3s$	2458	16365	18738	19887	21144	21931
	$4s$	2447	16367	18741	19889	21146	21239
	$5s$	2449	16369	18743	19891	20979	21148
$(YbCl_8Sr_{12})^{18+}$	Combined bases						
	Sr [$1s1p$] Interstice [$4s$]	2421	16111	18455	19573	20809	21039
	Sr [$5s1p$] Interstice [$4s$]	2207	16249	18594	19721	20968	19929

TABLE III: Results of the calculations on the $(YbCl_8Sr_{12})^{18+}$ cluster embedded in $SrCl_2$ with 96 valence electron correlation and relativistic effects up to spin-orbit coupling. Yb–Cl bond distances, R_e, in Å; totally symmetric vibrational frequencies, $\bar{\nu}_{a_{1g}}$, in cm^{-1}; minimum-to-minimum energy differences, T_e, relative to the $4f^{14}$–$1A_{1g}$ ground state, in cm^{-1}; and analyses of the spin-orbit wave functions. Manifold averages and mean square deviations of the individual values with respect to the averages are labeled as $\langle R_e \rangle$ and $\langle \bar{\nu}_{a_{1g}} \rangle$.

state	R_e	$\bar{\nu}_{a_{1g}}$	T_e	Percentage of spin-orbit free character [1]							
1 A_g	2.955	189	0	99.96	1 $^1A_{1g}$						
				$4f^{13}(7/2)5d(e_g)$ submanifold							
				$\langle R_e \rangle = 2.899 \pm 0.003$; $\langle \bar{\nu}_{a_{1g}} \rangle = 204 \pm 4$							
1 E_u	2.906	197	27781	89.32	1 $^3T_{1u}$	7.45	1 $^3T_{2u}$				
1 T_{2u}	2.906	196	27828	90.63	1 $^3T_{1u}$						
2 T_{2u}	2.898	208	30332	66.27	1 $^3T_{2u}$	29.39	1 $^1T_{2u}$				
1 A_{2u}	2.897	210	30357	97.97	1 $^3T_{2u}$						
1 T_{1u}	2.900	203	30598	40.37	1 $^3T_{1u}$	20.06	1 $^3T_{2u}$	19.55	2 $^1T_{1u}$	12.61	1 $^1T_{1u}$
2 E_u	2.900	203	31125	33.72	1 ^1E_u	32.82	2 $^3T_{1u}$	27.19	1 $^3T_{2u}$		
1 A_{1u}	2.899	206	31151	98.26	2 $^3T_{1u}$						
2 T_{1u}	2.899	205	31269	77.46	2 $^3T_{1u}$	7.18	2 $^1T_{1u}$				
3 T_{2u}	2.900	203	31538	36.65	1 ^3E_u	29.80	2 $^3T_{1u}$	21.26	1 $^1T_{2u}$	9.01	1 $^3T_{2u}$
3 T_{1u}	2.900	200	31606	47.25	1 ^3E_u	23.40	1 $^3T_{2u}$	18.18	1 $^1T_{1u}$		
3 E_u	2.898	207	32590	75.34	2 $^3T_{2u}$	11.20	1 ^1E_u	7.94	2 $^3T_{1u}$		
4 T_{1u}	2.896	207	32795	74.94	2 $^3T_{2u}$	12.99	1 $^1T_{1u}$	7.97	2 $^1T_{1u}$		
4 T_{2u}	2.894	209	33058	46.94	2 $^1T_{2u}$	26.60	2 $^3T_{2u}$	13.72	2 $^3T_{1u}$	6.76	1 ^3E_u
				interacting $4f^{13}(5/2)5d(e_g)$ and $4f^{13}(7/2)5d(t_{2g})$ submanifolds							
4 E_u	2.963	183	37305	84.27	3 $^3T_{1u}$	6.87	1 $^3T_{2u}$				
5 T_{2u}	2.963	184	37343	85.34	3 $^3T_{1u}$						
5 T_{1u}	2.944	159	38103	37.49	1 $^3T_{1u}$	19.11	3 $^3T_{1u}$	11.98	2 $^1T_{1u}$	8.58	1 $^1T_{1u}$
				7.86	5 $^1T_{1u}$	5.82	3 $^3T_{2u}$				
2 A_{1u}	2.906	195	38163	94.37	1 $^3T_{1u}$						
6 T_{2u}	2.965	179	39920	36.46	2 ^3E_u	25.69	4 $^3T_{1u}$	25.27	3 $^1T_{2u}$		
5 E_u	2.966	159	40023	36.81	2 ^1E_u	33.15	4 $^3T_{1u}$	16.42	3 $^3T_{2u}$		
6 T_{1u}	2.967	179	40105	65.39	4 $^3T_{1u}$	14.76	2 ^3E_u				

3 A_{1u}	2.967	185	40194	90.64	4 $^3T_{1u}$						
2 A_{2u}	2.969	181	40269	91.35	3 $^3T_{2u}$						
7 T_{2u}	2.969	174	40484	65.93	3 $^3T_{2u}$	10.69	3 $^1T_{2u}$	6.38	4 $^3T_{1u}$	5.43	5 $^3T_{1u}$
7 T_{1u}	2.944	164	40540	25.18	1 $^3T_{2u}$	22.11	3 $^1T_{1u}$	10.44	2 ^3E_u	10.25	4 $^3T_{1u}$
				8.65	3 $^3T_{1u}$	6.67	1 ^3E_u				
6 E_u	2.927	194	40623	43.61	1 $^3T_{2u}$	16.67	2 $^3T_{1u}$	12.05	1 ^1E_u	6.11	3 $^3T_{2u}$
				5.34	5 $^3T_{1u}$						
8 T_{1u}	2.948	200	41142	30.81	2 ^3E_u	13.37	1 $^3T_{2u}$	10.71	1 ^3E_u	10.69	3 $^1T_{1u}$
				9.21	3 $^3T_{1u}$	7.74	4 $^3T_{2u}$				
8 T_{2u}	2.969	148	41479	40.22	4 $^3T_{2u}$	37.76	1 $^3A_{2u}$	8.68	2 $^3T_{2u}$	5.23	3 ^3E_u
9 T_{2u}	2.926	157	41624	35.41	1 $^1T_{2u}$	15.12	1 $^3T_{2u}$	11.44	1 ^3E_u	10.55	2 $^3T_{1u}$
				6.23	1 $^3T_{1u}$	5.06	3 $^3T_{2u}$				
10 T_{2u}	2.924	243	41781	41.54	2 $^3T_{1u}$	33.35	1 ^3E_u	14.12	2 $^1T_{2u}$		
7 E_u	2.898	180	41988	39.43	1 ^1E_u	35.66	2 $^3T_{1u}$	15.19	2 $^3T_{2u}$		
8 E_u	2.950	197	42533	47.65	5 $^3T_{1u}$	30.70	3 ^1E_u	6.44	3 $^3T_{2u}$	5.29	1 $^3T_{2u}$
9 T_{1u}	2.961	186	42536	40.65	4 $^3T_{2u}$	24.93	3 ^3E_u	10.29	3 $^1T_{1u}$	6.90	1 ^3E_u
				5.42	1 $^1T_{1u}$						
10 T_{1u}	2.951	171	42769	20.16	4 $^1T_{1u}$	16.88	3 ^3E_u	16.12	5 $^3T_{1u}$	13.71	3 $^3T_{2u}$
				12.30	1 $^1T_{1u}$						
9 E_u	2.966	205	43007	56.97	4 $^3T_{2u}$	17.57	3 ^1E_u	12.61	2 ^1E_u	5.72	4 $^3T_{1u}$
				5.04	5 $^3T_{1u}$						
3 A_{2u}	2.900	195	43151	78.12	2 $^3T_{2u}$	12.88	1 $^1A_{2u}$	5.19	4 $^3T_{2u}$		
11 T_{1u}	2.931	143	43163	28.08	2 $^1T_{1u}$	27.50	1 $^3A_{1u}$	9.26	5 $^3T_{1u}$	7.58	1 $^3T_{2u}$
				6.10	4 $^1T_{1u}$	5.08	2 $^3T_{2u}$				
4 A_{1u}	2.966	183	43183	48.32	1 $^1A_{1u}$	35.06	5 $^3T_{1u}$	7.62	3 $^3T_{1u}$	6.74	4 $^3T_{1u}$
11 T_{2u}	2.924	162	43365	21.77	5 $^3T_{1u}$	20.50	2 $^3T_{2u}$	18.22	4 $^1T_{2u}$	16.21	1 $^3A_{2u}$
				11.84	2 $^1T_{2u}$	6.75	2 ^3E_u				
12 T_{1u}	2.942	222	43507	21.87	4 $^1T_{1u}$	17.59	1 $^1T_{1u}$	14.00	1 ^3E_u	8.82	4 $^3T_{2u}$
				8.37	2 $^3T_{1u}$	7.55	3 $^3T_{2u}$	7.53	2 $^3T_{2u}$	5.73	1 $^3A_{1u}$
12 T_{2u}	2.966	178	43752	42.23	3 ^3E_u	14.98	5 $^3T_{1u}$	12.45	4 $^1T_{2u}$	9.26	3 $^1T_{2u}$
				7.78	4 $^3T_{1u}$	5.38	1 $^3A_{2u}$				
13 T_{2u}	2.937	222	44025	35.13	2 $^3T_{2u}$	21.65	2 $^1T_{2u}$	13.67	5 $^3T_{1u}$	11.23	4 $^1T_{2u}$
				5.88	2 ^3E_u						
4 A_{2u}	2.952	201	44489	47.28	4 $^3T_{2u}$	29.14	1 $^1A_{2u}$	19.25	2 $^3T_{2u}$		
13 T_{1u}	2.945	186	45076	21.84	5 $^3T_{1u}$	16.57	1 $^3A_{1u}$	15.44	3 $^3T_{1u}$	12.81	5 $^1T_{1u}$
				12.71	2 $^1T_{1u}$						

interacting $4f^{13}(5/2)5d(t_{2g})$ and $[4f^{13}(7/2)a_{1g}^{YbTE} - 4f^{13}(7/2)6s]$ submanifolds

5 A_{1u}	2.969	183	47118	88.44	3 $^3T_{1u}$	8.49	1 $^1A_{1u}$				
10 E_u	3.079	194	48218	50.31	4 $^3T_{1u}$	24.57	3 $^3T_{2u}$	8.47	3 ^1E_u	7.46	2 ^1E_u

14 T_{2u}	3.069	225	48288	33.84	2 $^3A_{2u}$	32.80	5 $^3T_{2u}$	14.88	4 $^3T_{1u}$	6.35	2 ^3E_u
14 T_{1u}	3.071	224	48309	28.40	3 $^3T_{1u}$	25.68	5 $^1T_{1u}$	22.29	3 $^3T_{2u}$	13.16	2 ^3E_u
6 A_{1u}	3.057	275	48433	99.96	6 $^3T_{1u}$						
5 A_{2u}	3.074	184	48700	52.07	2 $^1A_{2u}$	45.53	5 $^3T_{2u}$				
15 T_{1u}	3.076	230	48801	51.49	6 $^3T_{1u}$	47.33	5 $^3T_{2u}$				
15 T_{2u}	3.073	197	48828	35.16	4 $^3T_{1u}$	15.99	5 $^3T_{2u}$	13.87	2 ^3E_u	8.77	2 $^3A_{2u}$
				5.84	6 $^3T_{1u}$	5.40	3 ^3E_u				
16 T_{1u}	3.011	273	49905	46.15	6 $^1T_{1u}$	26.64	6 $^3T_{1u}$	18.13	5 $^3T_{2u}$		
11 E_u	2.980	259	50291	64.76	5 $^3T_{2u}$	34.98	6 $^3T_{1u}$				
16 T_{2u}	2.979	259	50612	39.61	3 $^1T_{2u}$	15.99	2 ^3E_u	15.40	3 $^3T_{2u}$	12.09	5 $^3T_{1u}$
				6.44	3 $^3T_{1u}$						
17 T_{2u}	2.981	256	50820	50.66	5 $^1T_{2u}$	27.73	6 $^3T_{1u}$	15.60	2 $^3A_{2u}$		
12 E_u	2.973	237	50862	34.03	2 ^1E_u	30.88	3 $^3T_{2u}$	19.58	4 $^3T_{2u}$	7.27	3 $^3T_{1u}$
17 T_{1u}	2.975	243	51298	43.58	5 $^1T_{1u}$	20.82	3 $^3T_{2u}$	12.96	2 ^3E_u	5.21	4 $^1T_{1u}$
18 T_{1u}	2.968	214	51854	33.46	3 $^1T_{1u}$	13.66	3 ^3E_u	12.37	4 $^3T_{1u}$	12.32	3 $^3T_{2u}$
				7.41	4 $^1T_{1u}$	6.96	2 ^3E_u				
18 T_{2u}	2.968	181	53012	35.89	3 ^3E_u	28.65	4 $^3T_{2u}$	16.82	5 $^3T_{1u}$	6.89	1 $^3A_{2u}$
6 A_{2u}	2.969	181	53218	53.44	1 $^1A_{2u}$	42.51	4 $^3T_{2u}$				
19 T_{2u}	2.967	183	53475	43.06	4 $^1T_{2u}$	22.70	1 $^3A_{2u}$	15.57	4 $^3T_{2u}$	8.63	5 $^3T_{1u}$
19 T_{1u}	2.967	183	53512	37.81	5 $^3T_{1u}$	18.14	1 $^3A_{1u}$	17.71	4 $^3T_{2u}$	11.33	3 ^3E_u
13 E_u	2.966	183	53560	37.34	5 $^3T_{1u}$	35.01	3 ^1E_u	14.45	4 $^3T_{2u}$	8.77	3 $^3T_{2u}$
20 T_{1u}	2.965	182	54064	30.74	4 $^1T_{1u}$	22.92	3 ^3E_u	22.38	1 $^3A_{1u}$	12.43	4 $^3T_{2u}$
7 A_{1u}	2.966	183	54067	58.33	5 $^3T_{1u}$	39.77	1 $^1A_{1u}$				

States with double-well potential energy surfaces

Long distance minimum: $4f^{13}(5/2)6s$ submanifold [2]
$\langle R_e \rangle = 3.077 \pm 0.002$; $\langle \bar{\nu}_{a_{1g}} \rangle = 181 \pm 5$

20 T_{2u}	3.078	176	58594	48.02	5 $^3T_{2u}$	25.98	2 $^3A_{2u}$	25.83	6 $^3T_{1u}$		
14 E_u	3.078	176	58601	64.90	6 $^3T_{1u}$	35.06	5 $^3T_{2u}$				
7 A_{2u}	3.074	187	58937	53.38	5 $^3T_{2u}$	46.52	2 $^1A_{2u}$				
21 T_{1u}	3.080	183	58995	47.96	6 $^1T_{1u}$	32.17	5 $^3T_{2u}$	19.81	6 $^3T_{1u}$		
21 T_{2u}	3.077	181	59048	46.90	5 $^1T_{2u}$	36.12	6 $^3T_{1u}$	15.59	2 $^3A_{2u}$		

Short distance minimum: $4f^{13}(5/2)a_{1g}^{YbTE}$ submanifold [3]
$\langle R_e \rangle = 2.789 \pm 0.001$; $\langle \bar{\nu}_{a_{1g}} \rangle = 244 \pm 9$

20 T_{2u}	2.789	236	63359	49.01	5 $^3T_{2u}$	37.03	2 $^3A_{2u}$	7.56	5 $^1T_{2u}$	6.36	6 $^3T_{1u}$
14 E_u	2.791	236	63461	64.59	6 $^3T_{1u}$	35.37	5 $^3T_{2u}$				
7 A_{2u}	2.790	257	63363	56.72	5 $^3T_{2u}$	43.24	2 $^1A_{2u}$				

21 T_{1u}	2.788	243	63582	44.32	6 $^1T_{1u}$	34.60	5 $^3T_{2u}$	21.05	6 $^3T_{1u}$
21 T_{2u}	2.788	247	63550	57.31	6 $^3T_{1u}$	37.07	5 $^1T_{2u}$		

[1] Weights larger than 5% are given. They have been calculated at R(Yb-Cl)=2.951 Å unless indicated otherwise.

[2] Weights have been calculated at R(Yb-Cl)=3.071 Å.

[3] Weights have been calculated at R(Yb-Cl)=2.750 Å.

TABLE IV: Analysis of the $5A_{1u}$, $6A_{1u}$, and $7A_{1u}$ spin-orbit excited states at different Yb–Cl distances. Only the weights of spin-orbit free wave functions larger than 5% are given.

		Yb–Cl distance (Å)											
		2.70	2.75	2.80	2.84	2.89	2.93	2.95	2.98	3.02	3.07	3.12	3.16
State	Spin-orbit free component	Weights of spin-orbit free wave functions											
$5A_{1u}$													
	$4f^{13}5d(t_{2g})$												
	$1\ ^1A_{1u}$			7.56	7.96	8.24	8.41	8.49	8.60	8.79			
	$3\ ^3T_{1u}$			90.46	89.71	89.11	88.65	88.44	88.13	87.55	19.02		
	$4f^{13}a_{1g}^{YbTE} - 4f^{13}6s$												
	$6\ ^3T_{1u}$	99.97	99.97								78.35	99.91	99.88
$6A_{1u}$													
	$4f^{13}5d(t_{2g})$												
	$5\ ^3T_{1u}$					57.78							
	$1\ ^1A_{1u}$	6.68	7.17			40.05					7.16	9.16	9.34
	$3\ ^3T_{1u}$	91.96	91.17								67.98	86.33	
	$4f^{13}a_{1g}^{YbTE} - 4f^{13}6s$												
	$6\ ^3T_{1u}$			99.97	99.96		99.96	99.96	99.96	99.94	21.61		
$7A_{1u}$													
	$4f^{13}5d(t_{2g})$												
	$5\ ^3T_{1u}$	57.41	57.84	57.89	57.84		58.27	58.33	58.42	58.47	58.61	58.63	
	$1\ ^1A_{1u}$	40.66	40.26	40.23	40.27		39.83	39.77	39.67	39.62	39.47	39.44	
	$4f^{13}a_{1g}^{YbTE} - 4f^{13}6s$												
	$6\ ^3T_{1u}$					99.68							

FIG. 1: Partial representation of the crystal structure surrounding an Yb^{2+} substitutional impurity in $SrCl_2$. Yb^{2+}, at the center, appears surrounded by 8 Cl^-, 12 Sr^{2+} [at ($\frac{1}{2}$,$\frac{1}{2}$,0) sites] and 56 Cl^- ions in the first, second, and third coordination shells, respectively. The ions in the $YbCl_8$ moiety have been enhanced. Cl_8 cubes surrounding six of the twelve Sr^{2+} ions and one of the six empty interstitial sites [at ($\frac{1}{2}$,0,0) sites] are shaded in blue and grey, respectively.

FIG. 2: Breathing mode potential energy curves of the states of the $(YbCl_8Sr_{12})^{18+}$ cluster embedded in $SrCl_2$ with dominant configurational character $4f^{14}$ (black), $4f^{13}5d(e_g)$ (red), $4f^{13}5d(t_{2g})$ (blue), and $[4f^{13}a_{1g}^{YbTE}$– $4f^{13}6s]$ (green), in increasing energy order. All results include $SrCl_2$ host embedding and scalar relativistic effects. (a): Non-dynamic correlation, spin-orbit free, CASSCF($4f$,$5d$,$6s$) results. Dashed lines are used for 5^1T_{1u} and 6^1T_{1u} energy curves. Inset: RASSCF energy curves of the ground and 1 to 3 $^3A_{2u}$ states. (b): Non-dynamic and dynamic correlation of 96 valence electrons, spin-orbit free, MS-CASPT2(Cl64,Yb32) results. (c): 96 valence electron correlation plus spin-orbit, sfss-SO-CI results. States with strong mixing of configurational character are shown in black. (d) and (e) show only the ground state and the $^1T_{1u}$ states of (a) and (b), respectively. (f) shows the ground state and the T_{1u} states of (c). See text for details.

FIG. 3: Effects of extensions to the Yb($14s10p10d8f3g$)/[$6s5p6d4f1g$], Cl($7s7p1d$)/[$3s4p1d$] basis set on the 1 $^1A_{1g} \rightarrow 2\ ^3A_{2u}$ vertical transition energy calculated at R(Yb–Cl)=2.75 Å. Diamonds: $(YbCl_8Sr_{12})^{18+}$ embedded cluster calculations; $1s$ – $4p$ orbitals of Sr^{2+} are frozen and represented by embedding AIMPs; Sr $5s$ and $4p$ orbitals are added to the basis set contracted as [ns1p]. Bullets: $(YbCl_8)^{6-}$ embedded cluster calculations; n s-type primitive Gaussian functions are added at the ($\frac{1}{2}$,0,0) interstices. Triangles: $(YbCl_8Sr_{12})^{18+}$ embedded cluster calculations using the Sr [ns1p] and Interstice [$4s$] extensions. All the calculations are done at the CASSCF($4f$,$5d$,$6s$) level. The transition energies are referred to their values computed without the cluster and basis set extensions. See text for details.

FIG. 4: (a): Energy curves of the ground $^1A_{1g}$ and excited 2 $^3A_{2u}$ states. (b): $6s$ atomic natural orbital of the $4f^{13}6s^1$–^3F_u excited state of Yb^{2+} ion in the gas phase; Cl, Sr, Int (for interstice) labels have been plotted at the coordinates where they appear in plot (d) in order to set visual references. (c): a_{1g} molecular natural orbital of the $4f^{13}a_{1g}$–2 $^3A_{2u}$ state of the $(YbCl_8Sr_{12})^{18+}$ cluster calculated at R(Yb–Cl) = 2.75 Å, plotted in the diagonal plane of the Cl_8 cube. (d): same as (c) for R(Yb–Cl) = 3.18 Å. See text for details. Step of contour lines in (b)–(d) is 0.005. Last plotted contour line value is 0.005.

FIG. 5: Breathing mode potential energy curves of the excited states of the $(YbCl_8Sr_{12})^{18+}$ cluster embedded in $SrCl_2$. Quantum mechanical host embedding, 96 valence electron correlation, scalar relativistic, and spin-orbit effects are included in the calculations. All states are plotted together on the top, left. States of a given $\overline{O}_h$ irreducible representation are plotted in the remaining graphs, as indicated. States with a dominant configuration are plotted in color [$4f^{13}5d(e_g)^1$ (red), double-well $4f^{13}a_{1g}^{YbTE} - 4f^{13}6s^1$ (green)], those with strong configurational mixing are plotted in black. States $6A_{1u}$ and $5A_{2u}$ are plotted with dashed lines to help the discussion. Three auxiliary horizontal lines are plotted at 37000, 46000, and 58000 cm^{-1}. See text for details.

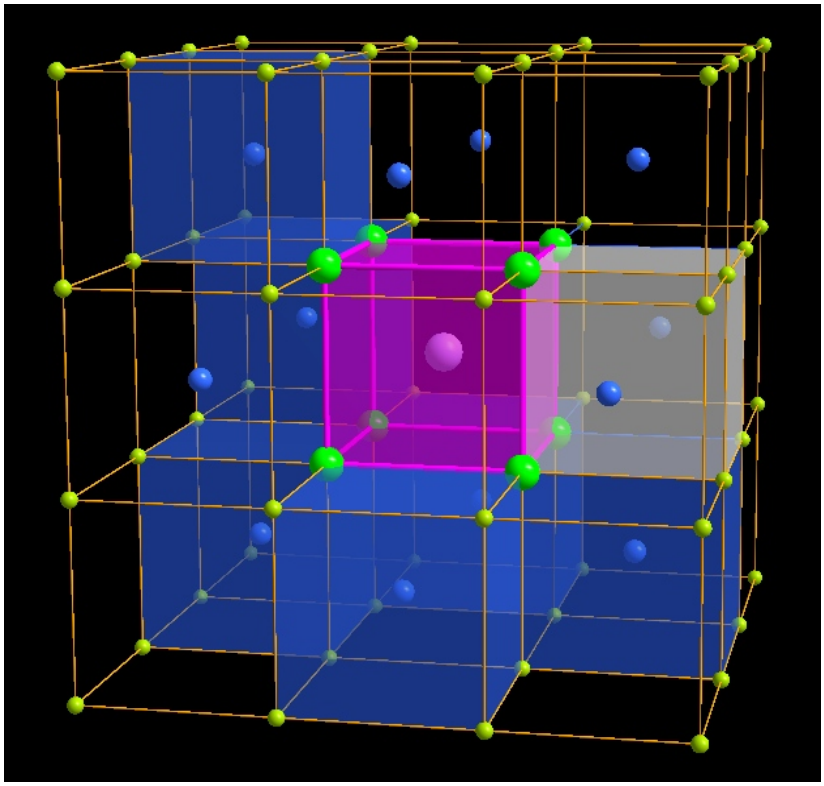

Figure 1. Sánchez-Sanz *et al.*, The Journal of Chemical Physics

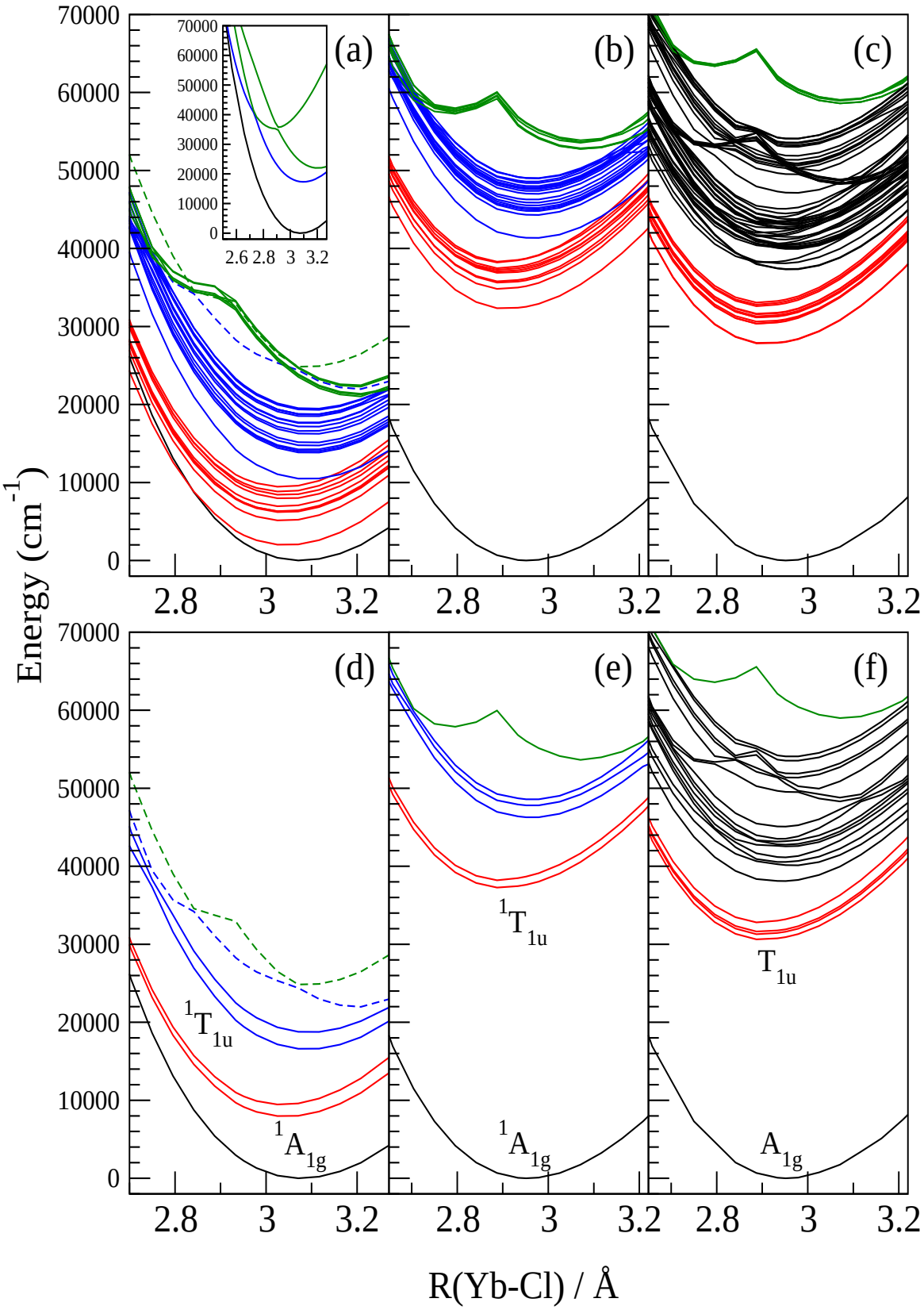

Figure 2. Sánchez-Sanz *et al.*, The Journal of Chemical Physics

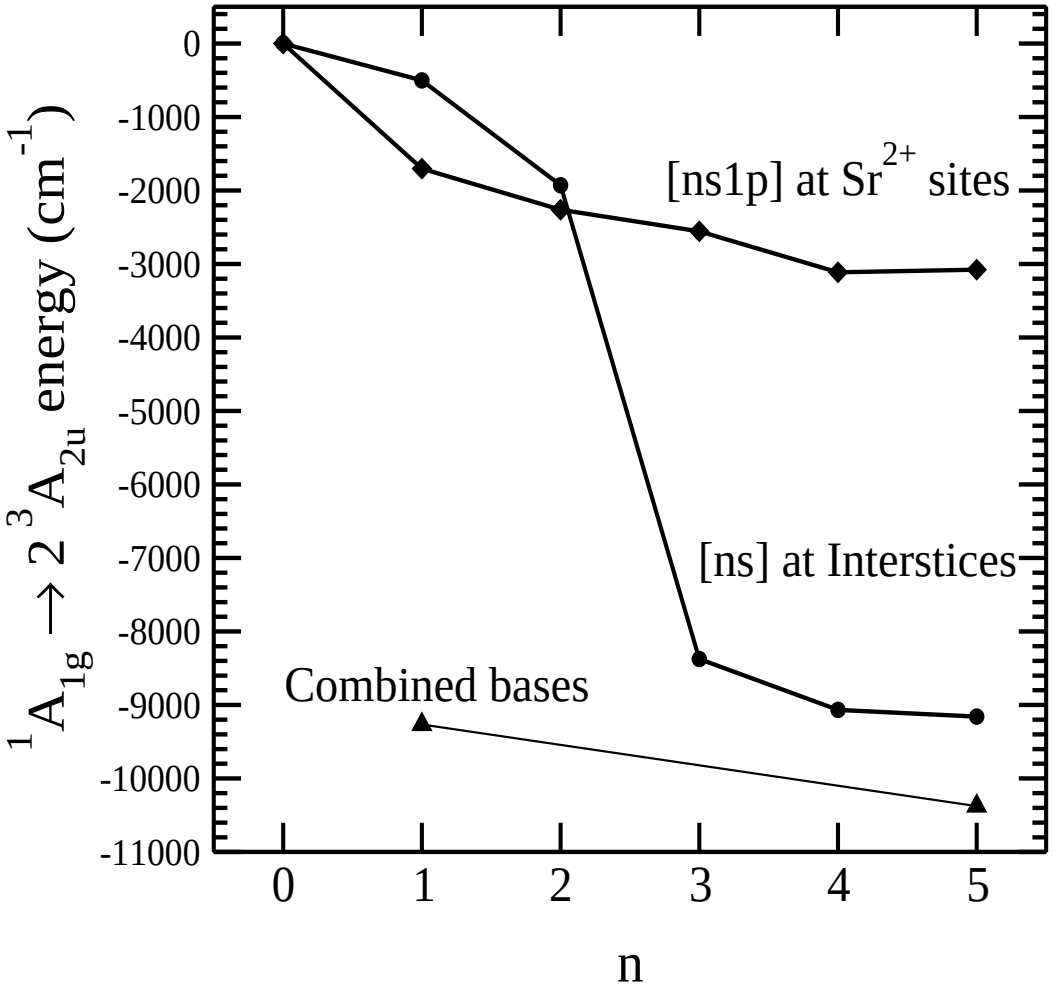

Figure 3. Sánchez-Sanz *et al.*, The Journal of Chemical Physics

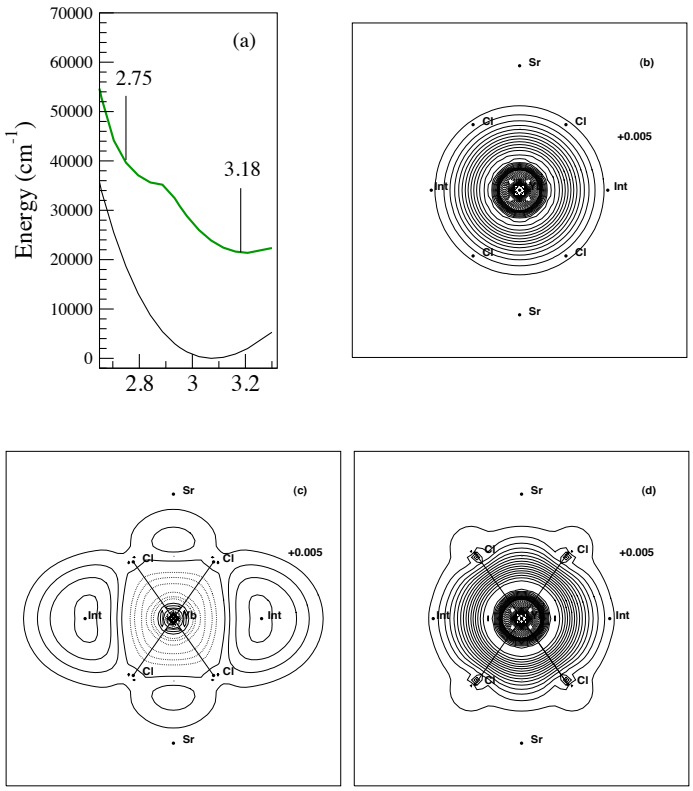

Figure 4. Sánchez-Sanz *et al.*, The Journal of Chemical Physics

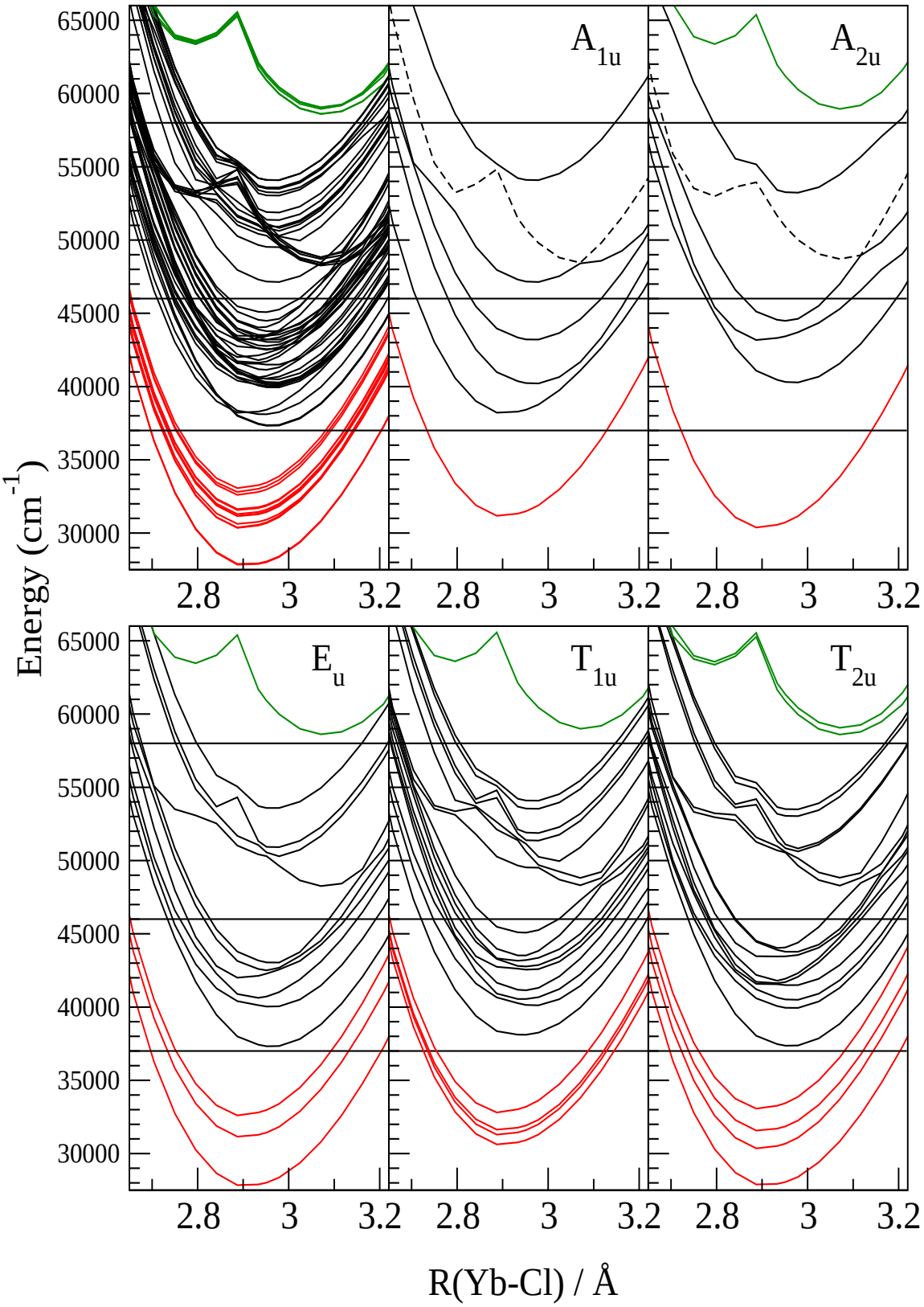

Figure 5. Sánchez-Sanz *et al.*, The Journal of Chemical Physics